11-10-2018

Calibration and Analysis of a Multimodal Micro-CT and Structured Light Imaging System for the Evaluation of Excised Breast Tissue.

David M. McClatchy III
Dartmouth College

Elizabeth J. Rizzo
Dartmouth College

Jeff Meganck
PerkinElmer Inc.

Josh Kempner
PerkinElmer Inc.

Jared Vicory
Kitware Inc

See next page for additional authors

Authors
David M. McClatchy III, Elizabeth J. Rizzo, Jeff Meganck, Josh Kempner, Jared Vicory, Wendy A. Wells, Keith D. Paulsen, and Brian W. Pogue

HHS Public Access

Author manuscript

Phys Med Biol. Author manuscript; available in PMC 2018 November 10.

Published in final edited form as:

Phys Med Biol. ; 62(23): 8983–9000. doi:10.1088/1361-6560/aa94b6.

Calibration and analysis of a multimodal micro-CT and structured light imaging system for the evaluation of excised breast tissue

David M. McClatchy III[1], **Elizabeth J. Rizzo**[2], **Jeff Meganck**[3], **Josh Kempner**[3], **Jared Vicory**[4], **Wendy A. Wells**[2,5], **Keith D. Paulsen**[1,5], and **Brian W. Pogue**[1,5]

[1]Thayer School of Engineering, Dartmouth College, 14 Engineering Dr., Hanover, NH 03755

[2]Department of Pathology, Dartmouth Hitchcock Medical Center, 1 Medical Center Dr., Lebanon, NH 03756

[3]PerkinElmer Inc., 68 Elm St. Hopkinton, Massachusetts 01748

[4]Kitware Inc., 101 E Weaver St, Carrboro, NC 27510

[5]Norris Cotton Cancer Center, Dartmouth Hitchcock Medical Center, 1 Medical Center Dr., Lebanon, NH 03756

Abstract

A multimodal micro-computed tomography (CT) and multi-spectral structured light imaging (SLI) system is introduced and systematically analyzed to test its feasibility to aid in margin delineation during breast conserving surgery (BCS). Phantom analysis of the micro-CT yielded a signal-to-noise ratio (SNR) of 34, a contrast of 1.64, and a minimum detectable resolution of 240 μm for a 1.2 min scan. The SLI system, spanning wavelengths 490 nm to 800 nm and spatial frequencies up to 1.37 mm^{-1}, was evaluated with aqueous tissue simulating phantoms having variations in particle size distribution, scatter density, and blood volume fraction. The reduced scattering coefficient, μ_s' and phase function parameter, γ, were accurately recovered over all wavelengths independent of blood volume fractions from 0% to 4%, assuming a flat sample geometry perpendicular to the imaging plane. The resolution of the optical system was tested with a step phantom, from which the modulation transfer function (MTF) was calculated yielding a maximum resolution of 3.78 cycles per mm. The three dimensional (3D) spatial co-registration between the CT and optical imaging space was tested and shown to be accurate within 0.7 mm. A freshly resected breast specimen, with lobular carcinoma, fibrocystic disease, and adipose, was imaged with the system. The micro-CT provided visualization of the tumor mass and its spiculations, and SLI yielded superficial quantification of light scattering parameters for the malignant and benign tissue types. These results appear to be the first demonstration of SLI combined with standard medical tomography for imaging excised tumor specimens. While further investigations are needed to determine and test the spectral, spatial, and CT features required to classify tissue, this study demonstrates the ability of multimodal CT/SLI to quantify, visualize, and spatially navigate breast tumor specimens, which could potentially aid in the assessment of tumor margin status during BCS.

1. Introduction

Breast conserving surgery (BCS) is common treatment for localized breast cancer, being less invasive than a full breast removal and having similar long term survival rates when combined with radiation therapy (Fisher et al. 2002). However, 20–40% of patients undergoing BCS endure follow-up re-excision procedures due to an incomplete original resection (Pleijhuis et al. 2009), as determined 1–2 days after the surgery through histopathology. Current standard of care includes intraoperative frozen section pathology and touch-prep cytology. Despite seeming diagnostic value, these procedures are extremely resource intensive to process and analyze just a small subset of the specimen, thus limiting widespread adoption (St John et al. 2017). With the high incidence of breast cancer, a critical need exists for surgical guidance tools to aid in assessing tumor involvement at the margin of a resected breast specimen during a BCS procedure in order to limit painful and costly re-excision procedures.

A plethora of biomedical devices have been proposed for this task, including electrical impedence spectroscopy (Kaufman et al. 2016), photoacoustic tomography (Wong et al. 2017), optical coherence tomography (Erickson-Bhatt et al. 2015), non-linear microscopy (Tao et al. 2014), dark field-confocal microscopy (Laughney et al. 2012), and Raman spectroscopy (Wang et al. 2016), among others. However, all of these methods either require exogenous dyes, chemically processing or fixing of tissue, or combing through point sampling volumes with a probe. But, a recently demonstrated imaging method, broadly referred to as high spatial frequency structured light imaging (SLI), has shown label free sensitivity to changes in freshly resected breast morphology over a large field of view (FOV) (~ 10^{0-2} cm^2) (McClatchy et al. 2016).

This approach, originally termed spatial frequency domain imaging (SFDI), was first demonstrated by Cuccia *et al.* to spatially map diffuse optical properties (Cuccia et al. 2005, Cuccia et al. 2009) and later applied to optical tomography (Bélanger et al. 2010), spectroscopic imaging (Gioux et al. 2011, Laughney et al. 2013), and fluorescence imaging (Sibai et al. 2015). The key advantage of structured illumination is the ability to tune depth sensitivity with the spatial modulation frequency. While the contrast at low spatial frequencies is dictated by absorption features (presence of blood, fat) and diffuse scattering (density of tissue), the contrast of sub-diffusive high spatial frequency images is dictated by both scattering intensity and the angular distribution of scattering events, or phase function, as photon propagation is constrained to superficial volumes with minimal volumetric averaging over tortuous photon path-lengths (Krishnaswamy et al. 2014, Bodenschatz et al. 2014). The phase function arises from the underlying physical properties of tissue ultrastructure (Bartek et al. 2006, Rogers et al. 2009, Radosevich et al. 2015). Recent studies have used sub-diffusive structured light imaging to quantify angular scattering distributions through the phase function parameter γ, which is related to the size-scale distribution of scattering features (Kanick et al. 2014, Bodenschatz et al. 2015). This phase function parameter, along with the reduced scattering coefficient μ_s', was used to cluster benign and malignant breast tissue pathologies in freshly resected human breast specimens (McClatchy et al. 2016) and morphologies within murine tumors (McClatchy et al. 2017), as different

tissue morphologies with unique densities and size-scale fluctuations manifest unique light scattering properties.

Although SLI can generate wide-field images of the specimen surface, it is unable to provide high resolution (< 1 mm) depth contrast or a tomographic reconstruction through the specimen volume. Micro-computed tomography (CT) is a promising technique for intraoperative visualization of breast specimens, which can be manufactured in a shelf shielded, mobile form factor. By reconstructing X-ray absorption in three dimensions (3D) thereby resolving overlaying features, micro-CT increases low contrast resolution relative X-ray projection imaging, and thus, yields a more accurate delineation of the tumor core extent and proximity to the margin in surgical breast specimens (Tang et al. 2013, Tang et al. 2016). Furthermore, micro-CT and SLI can be symbiotic as the former inherently loses image quality at the tissue-air interface, as the latter becomes the most sensitive.

In this manuscript, a novel multimodal imaging system, utilizing volumetric micro-CT and superficial SLI, is introduced and analyzed for future application in evaluation of excised breast tissues. Image quality and accuracy of both imaging modalities are assessed, as well as the co-registration of the two image systems. Accuracy of the optical property inversion method is validated on comprehensive sets of flat phantoms perpendicular to the imaging plane. As a proof-of-principle, an *exvivo* breast specimen is imaged during gross examination, yielding visualization of the tumor extent in 3D with co-registered structured light images and scatter parameter maps. Further work is needed to develop classification algorithms, at which point the clinical value of this multi-modality system can be tested.

2. Methods

2.1. Multimodal micro-CT & multi-spectral SLI system

The multimodal SLI/micro-CT system was created from a modified and repurposed IVIS SpectrumCT, which is a pre-clinical bioluminescence imaging and micro-CT system (PerkinElmer Inc., Hopkington, MA). The SLI addition consisted of the native IVIS charged coupled device (CCD) camera (Andor iKon, Andor Technologies Ltd., Belfast, UK) and a retrofitted digital light projector (DLP) (CEL5500 Fiber, Digital Light Innovations Inc., Austin, TX) with a 3.6× telephoto lens. Due to size constraints within the imaging cabinet, the DLP is rotated 22° with respect to the CCD, as shown in the schematic of the SLI system depicted in Fig. 1(a). Light was delivered through an optical fiber to the DLP, was focused onto the digital mirror device (DMD) creating the structured light patterns, and was then focused on the specimen. The DLP was connected to an external virtual monitor which controls the illumination pattern at a frame rate of 60 Hz. The illumination source was a supercontinuum laser (SuperK Blue, NKT Photonics, Denmark) with a tunable line filter (SuperK Varia, NKT Photonics, Denmark) to select the wavelength band. At the shelf stage height used for imaging, the diameter of the circular illumination field of the DLP was ~14 cm with a projection resolution of 168 μm, while the imaging field was ~26 cm × ~26 cm with a sampling resolution of 126 μm. Only a subset of the CCD corresponding to ~13 cm × ~13 cm covering the illumination field was read out to minimize acquisition time. The self-shielded micro-CT of the PerkinElmer system was a cone-beam CT in a ”pancake” geometry, with the specimen rotating through 360° on a turntable as shown in Fig. 1(b).

2.2. Data acquisition and processing

For the multimodal acquisition, micro-CT and SLI data were sequentially acquired with separate software packages. The specimen was placed on the rotation stage shown in Fig. 1(b), and the micro-CT scan was natively acquired and reconstructed through the PerkinElmer Living Image software. A 1 mA current was used and the tube peak kilovoltage (kVp) and exposure time were set to either 25 kVp and 200 ms/exposure or 50 kVp and 100 ms/exposure, yielding 2.4 min and 1.2 min total scan times for the low and high energy settings, respectively. The filtered back-projection reconstruction time was ~2 min for a reconstructed FOV of 12 cm × 12 cm × 3 cm with 150 micron cubic voxels.

After the micro-CT scan was completed, an SLI acquisition occurred with a custom LabView routine (National Instruments, Inc., Austin, TX). For all scans in this study, seven wavelengths were acquired, λ = [490, 550, 600, 650, 700, 750, 800] nm, with a 15 nm bandwidth, and at each wavelength, 18 one-dimensional sinusoidal projections were recorded at 6 spatial frequencies, f_x = [0.05, 0.15, 0.61, 0.78, 0.92, 1.37] mm^{-1} with 3 phase offsets, ϕ = [0, 120, 240]°. Although previous research has shown sensitivity of the rotation angle of the modulation pattern to oriented features (DAndrea et al. 2010, Konecky et al. 2011), in this protocol only one rotation angle was considered to minimize the time of a SLI scan, which was ~8 min for both acquisition and saving. After specimen scanning, an 8 in. × 8 in. silicone TiO_2 phantom and a 10 in. × 10 in. 99% reflectance standard (Labsphere, Inc., Sutton, NH) were imaged for calibration.

SLI data processing occurred off-line with custom scripts in MATLAB (2016a). Images were demodulated by $I_d = \frac{\sqrt{2}}{3}\sqrt{(I_{\phi 1}-I_{\phi 2})^2+(I_{\phi 1}-I_{\phi 3})^2+(I_{\phi 1}-I_{\phi 3})^2}$, where $I_{\phi 1}$, $I_{\phi 2}$, $I_{\phi 3}$ are the three phase offsets for a given spatial frequency and wavelength. Due to minor fluctuations in laser power, phase images were scaled so that each had the same mean over the illuminated area to minimize demodulation artifacts. Also, a median filter with 3×3 pixel kernel was applied to demodulated images to remove noise and any specular reflections arising from minor fluctuations of the tissue surface profile. These specular reflections were mitigated by flattening the tissue surface between two transparent acrylic plates and also using an oblique projection scheme. Optical property maps were calculated with a sub-diffusive model inversion method described in a previous manuscript (Kanick, Krishnaswamy, Gamm, Sterenborg, Robinson, Amelink & Pogue 2012, McClatchy et al. 2016). The sub-diffusive model was semi-empirically derived from a series of forward Monte-Carlo simulations utilizing a modified Henyey-Greenstein phase function (Kanick, Robinson, Sterenborg & Amelink 2012). To summarize briefly, demodulated images were calibrated by the TiO_2 phantom as

$$R_{d_{\text{sample}}}(x,y,f_x,\lambda) = R_{d_{\text{TiO}_2}}(x,y,f_x,\lambda)\frac{I_{d_{\text{sample}}}(x,y,f_x,\lambda)}{I_{d_{\text{TiO}_2}}(x,y,f_x,\lambda)},$$

where $R_{dTiO_2}(x, y, f_x, \lambda)$ are sub-diffusive model-predicted reflectance values for the calibration phantom. A non-linear least squares routine determined optical properties by minimizing the difference between measured calibrated reflectance and model-based predicted reflectance over all spatial frequencies and wavelengths. Scattering was assumed to follow a power law such that

$\mu_s' = A\left(\frac{\lambda}{800\text{nm}}\right)^{-B}$, where A, B are the scattering amplitude and power, respectively. The phase function parameter γ was a free fit variable at each wavelength. For tissue specimens, the absorption coefficient, μ_a, was assumed to be a linear sum of oxygenated hemoglobin, deoxygenated hemoglobin, and β-Carotene with basis spectra obtained from the Oregon Laser Medical Center (OLMC) spectra database (http://omlc.ogi.edu/spectra/index.html Accessed May 2017).

Color images were also reconstructed from the multi-spectral SLI data. For the 5 wavelengths in the visible spectrum, λ = [490, 550, 600, 650, 700] nm, SLI images were transformed into a RGB color-space using the 1931 International Commission on Illumination (CIE) tristimulus values (Smith & Guild 1931). For each illumination band, the x, y, z chromaticity values were calculated and normalized, and multiplied by the demodulated intensity of the specimen and the 99% reflectance standard for each respective wavelength band. The resulting x, y, z image stack was converted to RGB space with the value of the 99% reflectance standard set to be the white point.

2.3. 3D-2D co-registration and visualization

Accurate calibration and co-registration of the 2D image coordinates to the 3D CT coordinates are needed for a multimodal visualization. Camera calibration with the optical system was performed to account for lens and perspective distortion. This was done using the Open Source Computer Vision Library (OpenCV) Camera Calibration and 3D Reconstruction Software (*Open Source Computer Vision Library* Accessed June 2016), with which the intrinsic camera matrix and radial and tangential lens distortion coefficients were calculated. Images acquired were corrected using the *undistortImage* function in the MATLAB Computer Vision System Toolbox (version 2016a). The transformation matrix from the optical image coordinates to the CT coordinates in the XY plane was calculated using procrustes alignment method. Because the optical and micro-CT systems were rigidly fixed, these calibrations were performed once, and were used in all imaging experiments reported here.

With the optical system calibrated, a module was created to co-register and display an acquired CT/optical scan automatically which was integrated into NIRFAST Slicer software (http://www.dartmouth.edu/~nir/nirfast/) (Jermyn et al. 2013, Dehghani et al. 2009). A diagram of the data-processing and work-flow is shown in Fig. 2 for a hemispherical gelatin phantom. The height map was extracted from the CT volume by determining the most superficial CT voxel above a manual threshold, for each x, y vector of voxels. Next, the optical image was undistorted and then coregistered to CT coordinates through the linear transformation. Finally, for each point on the height map, the scalar value of the nearest optical data point was assigned. With this 3D scalar data, a triangular surface mesh was created in the Visualization Toolkit (VTK) file format, which was then simultaneously rendered with the CT volume in the Slicer environment (Taka & Srinivasan 2011).

2.4. Micro-CT, optical, & co-registration phantoms

To quantify image quality of the micro-CT system, a mammography target phantom (Mammo 156 Phantom, Gammex Inc., Middleton, WI) was utilized. This mammography accreditation phantom is composed of acrylic with a wax insert containing various fibers, hemispherical masses, and specs. It has been designed to simulate a compressed breast comprised of 50% glandular and 50% adipose tissue and size of 10.2 cm × 10.8 cm × 4.2 cm. While the phantom was larger than the micro-CT FOV, surgical specimens are smaller than the entire breast and contain less background tissue; thus, only the wax insert was imaged. Furthermore, if the entire phantom were imaged, partial volume artifacts would have greatly degraded image quality, with a large portion of phantom having been outside of the X-ray beam.

The spatial resolution of the SLI system was analyzed with a step phantom. A sheet of highly absorbing black paper was placed on a 99% reflectance standard creating a sharp edge between a highly reflective and nearly non-reflective surface. The spatial resolution was analyzed by characterizing the response of the imaging system across the edge.

To validate the sensitivity of the SLI system and accuracy of the optical property inversion method, two sets of tissue simulating aqueous phantoms were imaged. In the first set of phantoms, the size-scale distributions of scatterers were varied by selectively titrating various concentrations of Intralipid (IL) and a solution of 140 nm polystyrene spheres. The optical properties of the sphere solution was calculated with Mie theory (Bohren & Huffman 2008), while the optical properties of IL were taken from a previous publication (Michels et al. 2008), and a discrete particle model was used to calculate the optical properties of different ratios of each solution (Gélébart et al. 1996). The various solutions contained $\gamma \in$ [0.99 – 2.00] and μ_s' of each phantom was matched at λ = 650 nm. In the second set of phantoms, absorption and scattering were varied independently with various concentrations of IL and whole porcine blood (Lampire Biologicals, Pipersville, PA). The hemoglobin concentration of the blood was measured at 13.4 g/dl, and to maintain neutral pH, phosphate buffered was used for dilution. Solutions were made with [0.5,1,2] % IL and [0,0.5,1,2,4] % blood volume fractions (BVF), yielding phantoms with $\frac{\mu_s'}{\mu_a} \in [0.8 - 10^5]$ over the acquired wavelength range assuming fully oxygenated blood. The influence of blood on the scattering properties were considered to be negligible compared the influence of IL, based upon previous studies measuring the optical properties of blood (Friebel et al. 2006, Bosschaart et al. 2014). Each phantom set was imaged in a 24-well plate having black, non-transparent walls and 2.5 ml of each solution per well.

Accurate co-registration between the micro-CT and optical imaging system was experimentally validated and quantified with a custom-made phantom containing radio-opaque and optically bright markers. The markers were 1/8 in. acetal pins, the top surfaces of which were coated in commercial liquid paper to increase optical reflection. Two orthogonal lines of 7 markers with approximately 1 cm spacing were set on optically dark paper creating a cross-hair pattern. The co-registration accuracy was measured as the co-localization of the marker positions in the CT and SLI datasets.

2.5. Imaging a surgically resected breast specimen

To demonstrate feasibility of the system to acquire and display a multimodal clinical dataset, a freshly resected breast tissue specimen was scanned. The imaging protocol did not interfere with standard of care posing minimal risk to the patient, and was approved by the Dartmouth Hitchcock Medical Center (DHMC) Internal Review Board (IRB) and the Committee for the Protection of Human Subjects (CPHS). After a breast surgery specimen was received by the Department of Pathology, it was subsequently ”bread loafed” and grossly assessed per standard of care. Cut tissue specimens with superficial lesions were imaged with system, which was located in the surgical specimen lab. To maintain the orientation of the specimen through imaging and also provide a flat imaging surface, it was placed in a customized holder, consisting of two 1/8 in. thick, optically-clear acrylic plates, between which the specimen was secured with elastic bands. The silicone calibration phantom, having a refractive index similar to tissue (Ayers et al. 2008), was likewise imaged with the acrylic plate. Immediately after imaging, the specimen was cut into cassette sized sections (~1 cm), photographed, and underwent standard histological processing of dehydration, fixation, wax embedding, sectioning and hematoxylin and eosin (H&E) staining. Resulting histology was evaluated by a trained pathologist (W.A.W) and included in the patient’s report.

3. Results

3.1. Micro-CT analysis of mammography target phantom

The micro-CT target phantom analysis resulted in the same minimum detectable objects (*MDO*) for the low and high energy scans, with only the smallest fiber and smallest speck cluster not clearly visible. This yielded a limiting resolution of 240 μm for a high-contrast spherical object. To assess image quality of the micro-CT, the signal-to-noise ratio (*SNR*) and *Contrast* were evaluated for each kVp scan. A single slice through the largest mass was analyzed, with the mean, μ, and standard deviation, σ, of the linear attenuation coefficient calculated in a region of interest (ROI) in both the largest mass and in the abutting background. *SNR* was calculated as $SNR = \mu_{mass}/\sigma_{background}$ and $Contrast = \mu_{mass}/\mu_{background}$. The 50 kVp scan yielded an *SNR* of 34 for a 72 sec acquisition, while the 25 kVp scan yielded an SNR of only 23.8, despite compensating for higher attenuation by doubling the exposure time. The 25 kVp did have a slightly higher *Contrast* of 1.81, compared to 1.64 for the 50 kVp scan. A tabulated summary of the metrics quantifying the micro-CT performance is shown in Table 1. Because of the shorter scan time, superior *SNR*, and similar *Contrast*, subsequent micro-CT scans displayed this point forward were acquired with the 50 kVp, 100 ms/exposure scan settings.

3.2. Multi-spectral structured light imaging analysis

The spatial resolution of the demodulated intensity as a function of spatial frequency and wavelength was tested by analyzing the response of a step phantom. In Fig. 3(a), a captured image of the step phantom is shown for $f_x = 0$ mm^{-1} and $\lambda = 490$ nm. The direction of the illumination frequency is at a 68° angle with the step, while the y-axis of the CCD is parallel, so that the captured imaged can be averaged along the step. Measured edge responses across the step are shown for each imaged wavelength at $f_x = 0$ mm^{-1} in Fig. 3(b).

A forward difference approximation and subsequently a fast Fourier transform (FFT) was applied to each edge response to calculate the corresponding modulation transfer functions (MTF), shown in Fig. 3(c). Each MTF was normalized by its maximum value and smoothed with a 5 pixel moving average filter. Edge responses and MTFs are likewise shown in Fig. 3(d) and (e) respectively, for each imaged spatial frequency at λ = 490 nm. The limiting spatial resolution is quantified as the point where the MTF reaches 10% of its maximum value. These values are tabulated for the variation in wavelength and spatial frequency in Fig. 3(f). For the case of diffuse illumination, a clear trend of increasing spatial resolution from 2.24 cycles/mm to 3.17 cycles/mm, occurs as wavelength decreases from 800 nm to 490 nm. Although the reflectance standard is near completely reflective, this wavelength dependent behavior is still expected as the lower edge of the phantom will have a higher scattering cross section with shorter wavelength light, and therefore, a shorter transport length resulting in a sharper response. Also, as the spatial illumination frequency increases, a slight increase is found in spatial resolution, which is also expected as increasing the spatial illumination frequency constrains the light transport to become more superficial and localized, also resulting in a sharper response. Results revealed a maximum spatial resolution of 3.78 cycles/mm at λ = 490 nm and f_x = 1.37 mm^{-1}.

The sensitivity and accuracy of the SLI system was evaluated with aqueous tissue simulating phantoms, mimicking the expected contrast and background absorption in human breast tissue. Two sets of phantoms were characterized: a first set with variations in particle size scale distribution, and a second set with variations in BVF and IL concentration to alter both absorption and scattering, independently. The recovered values of γ and μ_s' for each particle size scale distribution are shown in Fig. 4(a) and (b), respectively. The magnitude of γ was unique over all wavelengths for each particle size scale distribution, with γ exhibiting a linear relationship with wavelength. The magnitude of γ decreased with the increasing contribution of the more isotropic 140 nm spheres compared to the more forward scattering IL. Likewise, the spectral slope of μ_s' also stratified for each particle size scale distribution, with an increasing slope for greater contributions of the 140 nm spheres and a flatter slope for IL. The greatest dynamic range for both γ and μ_s' to changes in particle size scale distribution appear to be towards the shorter wavelengths of light. The known versus recovered values of γ and μ_s' for each particle size distribution at each measured wavelength are plotted in Fig. 4(c) and (d) respectively. *Error* was calculated as $\text{Error} = 100 \times \frac{|\text{recovered} - \text{known}|}{\text{known}}$, and the mean and standard deviation were computed over all phantoms at each wavelengths, yielding $\langle 10 \pm 5.4 \rangle$% for γ and $\langle 5.77 \pm 6.6 \rangle$% for μ_s'. The recovered values of γ and μ_s' for variations in IL concentration and BVF are shown in Fig. 4(e) and (f) respectively. As expected, the recovered γ spectra cluster together, independent of both IL concentration and background absorption from BVF. Additionally, the magnitude of the μ_s' values stratify by the various IL concentrations, independent of the BVF. Plots of the corresponding known versus recovered values are presented in Fig. 4(c) and (d) for γ and μ_s', respectively. The mean error in recovering γ in the presence of various scattering and absorption concentrations was $\langle 4.8 \pm 3.1 \rangle$%, while the mean error for μ_s' was

⟨12 ± 7.4⟩%. These phantom studies experimentally validated the ability of the multi-spectral SLI system to accurately recover and quantify sub-diffusive scatter parameters accurately over a broad range of optical properties, which can be expected for surgical tissues in the visible to NIR wavelength bands.

3.3. Optical & micro-CT co-registration accuracy

Co-registration accuracy between the micro-CT imaging space and optical imaging spaces was evaluated and quantified. A phantom with radio-opaque pegs having an optically bright coating, shown in Fig. 5(a), was measured with the multimodal system, yielding a micro-CT scan and a co-registered 3D surface mesh of SLI reflectance data. The micro-CT and SLI data were manually thresholded to segment the surface pegs. A top down 2D view of the segmented CT and optical mesh points is presented in Fig. 5(b). A zoomed in view of the center peg is shown in Fig. 5(c), where individual locations are shown with an apparent offset of a few points, each being 150 μm apart. In Fig. 5(d), the segmented CT and optical mesh points are plotted in 3D, showing the minor error in co-registration resulting in slight misalignment. The co-registration accuracy is quantified for each peg as the Euclidean distance in *x, y, z* between the centroids of the CT surface and the optical mesh surface. These results are tabulated in Table 2, and shown a mean co-registration accuracy of 620 μm with little variation across the coordinate space. Furthermore, this implies that in future studies, optical and CT data of breast cancer specimens can be spatially interpreted together within a range 620 μm.

3.4. Visualization of a freshly resected breast tissue specimen

Illustrative multimodal data of a freshly resected breast specimen are shown in Fig. 6. A photograph of the cut specimen appears in Fig. 6(a) with tessellated H&E stained histology slides displayed in 6(b). Evaluation of the histology from a trained pathologist (W.A.W) revealed a 2.5 cm lesion of invasive and *in-situ* lobular carcinoma with adjacent, benign fibrocystic disease (FCD) surround by background adipose. While the background adipose exhibits a shade of yellow in the photograph, the invasive versus benign areas both appeared in shades of white. The demodulated intensity is shown at f_x = [0, 1.37] mm^{-1} for λ = 490 nm in Fig. 6(c) and (d) respectively and for λ = 600 nm in Fig. 6(e) and (f), respectively. For the diffuse images at f_x = 0 mm^{-1}, significantly more contrast occurred between the glandular tissue and adipose for λ = 490 nm compared to the longer wavelengths, due to absorption from β-Carotene. However, the superficial high-spatial frequency images at f_x = 1.37 mm^{-1}, revealed similar spatial features for both the shorter and longer wavelengths. Contrast was further quantified over all wavelengths and spatial frequencies. Surfaces of the ratio of the demodulated intensity between tumor and adipose and between tumor and FCD are shown in Fig. 6(h) and (i), respectively, for the areas marked by arrows in Fig. 6(b). Tumor to adipose had much greater maximum contrast of 5.6 than tumor to FCD, which had a maximum contrast of 1.6, because of the greater dissimilarity in tissue ultrastructure. For both ratios, contrast increased with spatial frequency with the maximum contrast occurring at f_x = 1.37 mm^{-1}, but at λ = 490 nm for tumor to adipose and at λ = 700 nm for tumor to FCD. In Fig. 6(j), axial and sagittal slices of the specimen are shown for the 50 kVp micro-CT scan. In the axial slice, the tumor mass and spiculations were visible. In the sagittal slice, micro-calcifications appeared as bright specks and the acrylic specimen holder was also

visible. A histogram showing the distribution of the measured linear attenuation coefficients of the tissue is shown in Fig. 6(k). Fat and glandular peaks were centered at 0.31 cm^{-1} and 0.435 cm^{-1} respectively, and yielded a *SNR* of 30.1 and *Contrast* of 1.40. While contrast was clearly visible between the glandular tissue and background, negligible contrast occurred within the glandular region between areas of tumor and FCD, unlike the SLI data.

Processed optical maps from the raw SLI reflectance data are presented in Fig. 7. A color image reconstructed from the visible diffuse images at $f_x = 0$ mm^{-1} is shown in Fig. 7(a) with green, black, and red boxes outlining regions of adipose, lobular carcinoma, and FCD, respectively. In 7(b), another color image reconstructed from visible demodulated data is displayed, but for a high spatial frequency of $f_x = 1.37$ mm^{-1} highlighting the superficial, finer spatial features. In Fig. 7(c), a map of the scatter slope of μ_s' is shown, which represents the spectral change in scattering intensity and is related to particle size distribution of scatters. The mean values of μ_s' versus wavelength are plotted in 7(d) for the three regions, with error bars representing the standard deviation within each region. The elevated scatter slope of FCD ($\langle 1.94 \pm 0.21 \rangle$) compared to that of carcinoma ($\langle 1.33 \pm 0.35 \rangle$) can be seen, as well as the characteristically flat scatter slope and low scatter magnitude of adipose ($\langle 0.53 \pm 0.21 \rangle$). Mean values of γ versus wavelength are plotted in 7(e), showing decreased values for FCD and carcinoma with little wavelength variation and increased values for adipose with an apparent negative linear relationship with wavelength (r=−.992). Spatial features of the optical properties can be observed in the various optical property maps. In Fig. 7(f) and (g), μ_s' maps and in Fig. 7(h) and (i) corresponding γ maps are shown for $\lambda = 490$ nm and 600 nm, respectively. For both μ_s' and γ, maximum contrast between the tumor and adipose is achieved at $\lambda = 490$ nm, but with minimal contrast between tumor and FCD. At $\lambda = 600$ nm, contrast between tumor and FCD increased for μ_s' and γ, while contrast between tumor and adipose decreased.

Superficial SLI and volumetric micro-CT data were simultaneously rendered in the open-source Slicer environment (Fedorov et al. 2012). A screen-shot of the multimodal display appears in Fig. 8. A false colored surface of $\mu_s'(490\ \mathrm{nm})$ is shown in Fig. 8(a), exhibiting spatial detail in optical scattering intensity. In Fig. 8(b), the μ_s' surface is shown co-registered to a maximum intensity projection of the micro-CT volume, which was processed with the Slicer Volume Rendering module to create a segmented semi-transparent object. Fat was made virtually transparent while the tumor mass and spiculations arms were more opaque. An apparent cluster of micro-calcifications, marked by a yellow star, appear as completely non-transparent, having a markedly high radio-density. The sagittal and coronal slices through the co-registered optical surface and micro-CT volume are displayed in Fig. 8(c) and (d), respectively. Standard navigation tools in the Slicer environment enabled annotation between the different views and planes. In Fig. 8(e), the diffuse color image is also shown to guide spatial recognition of features in the multimodal data set to how the specimen appears to the naked eye. In Fig. 8(f), axial micro-CT slices are shown in 0.9 mm steps below the imaging surfacing illustrating the overlapping structural features of the tissue. The micro-calcification cluster is shown to be 1.8 mm below surface and is marked with a yellow star.

A corresponding H&E section taken at 1.8 mm depth likewise shows a cluster of type-II micro-calcifications in Fig. 8(g)

4. Discussion

Results from both phantom experiments and clinical tissue demonstrated the ability of the micro-CT/SLI system to quantify scattering maps and co-register them with a micro-CT image volume. Target phantom analysis and specimen imaging with the micro-CT demonstrated $SNR > 30$, and sub-millimeter resolution. Micro-calcifications were detectable during specimen imaging, and while the presence of calcifications is not considered diagnostically relevant, microscopic pleomorphic calcifications can be related to malignancy status (Tse et al. 2008). Resolution tests of SLI also yielded sub-millimeter resolution, and tissue simulating phantoms demonstrated accuracy in the model inversion well beyond diffusion limited transport. While a previous study has accurately quantified optical properties in aqueous phantoms over a range of $\gamma \in [1.3 – 1.7]$ and $\frac{\mu_s'}{\mu_a}$ as low as 5.6 with modest accuracy (McClatchy et al. 2016), this study experimentally recovers $\gamma \in [0.99 – 2.00]$ and $\frac{\mu_s'}{\mu_a}$ as low as 0.8 with double the accuracy in μ_s' recovery. Imaging of the breast specimen demonstrated co-localization of scattering information with a volumetric micro-CT scan. Imaging irregular specimen surfaces may pose a challenge in the future studies aimed at whole specimen imaging; however, if flattening the tissue surface with the custom acrylic holder does not suffice, a recently published modified Lambertian model has shown to effectively mitigate surface curative artifacts in spatial frequency domain imaging applications (Zhao et al. 2016).

The preliminary data suggests SLI and micro-CT are likely to be complementary, as the micro-CT lacks contrast between benign and malignant glandular tissues but provides a 3D reconstruction of the tumor core within a specimen, whereas SLI offers enhanced superficial contrast between more subtle morphological changes. Sensitivity to the surface of tissue is substantiated by a current consensus report which states that ”no tumor on ink” is appropriate for early stage invasive breast cancer (Buchholz et al. 2014). With this work flow, the micro-CT could guide selection of surfaces to be optically imaged and provide the proximity of suspicious lesions to the tumor mass. Additionally, contextualizing SLI measurements with the subsurface proximity of the tumor-core, as calculated from the micro-CT, could potentially aid in interpretation of the multimodal data.

Future development of this technology will require creation of a robust classification model to determine margin status based on the multimodal data. A previous study has shown optical scattering parameters of freshly resected human breast tissue recovered with sub-diffusive structured light are sensitive to changes in tissue morphology (McClatchy et al. 2016). However, with model based inversion methods, fitting time is a limitation. While look-up-table approaches could provide a substantial improvement, a direct calculation of optical properties from an empirically fitted function has demonstrated faster inversion times without the need for a look-up routine (Angelo et al. 2016). A classification model based on raw multi-spectral reflectance over multiple spatial frequencies may overcome the

computational barrier. Previous research has used raw spatial frequency images captured at multiple rotation angles to map the alignment of avian muscle tissue (Konecky et al. 2011). This technique could potentially be useful in determining the degree of stromal alignment in breast specimens, which could be related to disease progression (Provenzano et al. 2006, Conklin et al. 2011). Furthermore, spatial and spectral analysis of raw reflectance images of excised breast tissue have offered great diagnostic potential in a dark-field confocal microscopy configuration, where scatter contrast was enhanced similarly to high-spatial frequency SLI (Laughney et al. 2012, Pardo et al. 2017). With future development of a classification model validated with histopathology, the technology described here can be evaluated in the clinical theater.

5. Conclusions

In this manuscript, a novel multimodal imaging system combining superficial SLI and volumetric micro-CT was systematically evaluated in phantoms, and as a proof-of-principle, a freshly excised human breast specimen was scanned. To the authors knowledge, these results appear to be the first demonstration of SLI or SFDI combined with a standard medical tomography system for imaging excised tumor specimens. System performance quantified through the phantom experiments suggests that the contrast, resolution, SNR, and co-registration accuracy needed for surgical guidance can be obtained within a time frame meeting clinical work flow requirements. The preliminary breast specimen imaging further suggests that the system could aid in visualization of a resected specimen. Further studies in a large cohort of resected specimens are needed to determine the optimal spatial, spectral, and tomographic features required for assessment of margin status before the system can be clinically evaluated.

Acknowledgments

This work was funded through National Institutes of Health (NIH) Academic-Industrial Partnership grant R01CA192803 awarded by the National Cancer Institute (NCI) to Dartmouth College and PerkinElmer. The development and analysis of the SLI imaging system was in part funded by NIH/NCI grant F31CA196308 supporting DMM. We would like to disclosure that authors JM and JK are employees of PerkinElmer Life Sciences Inc., who make products used in this research. Also, the Slicer module described in this research was developed through a subcontract with Kitware Inc., of which author JV is an employee. The authors would like to thank Dr. Stephen Kanick, Dr. Jonathan Elliott, Dr. Venkataramanan Krishnaswamy, Dr. Samantha Horvath, and Dr. Andinet Enquobahrie for helpful discussions.

References

Angelo J, Vargas CR, Lee BT, Bigio IJ, Gioux S. Journal of Biomedical Optics. 2016; 21(11):110501–110501. [PubMed: 27901550]

Ayers F, Grant A, Kuo D, Cuccia DJ, Durkin AJ. Proc. SPIE. 2008; 6870:687007–9.

Bartek M, Wang X, Wells W, Paulsen KD, Pogue BW. J Biomed Opt. 2006; 11(6):064007. [PubMed: 17212530]

Bélanger S, Abran M, Intes X, Casanova C, Lesage F. Journal of biomedical optics. 2010; 15(1): 016006–016006. [PubMed: 20210452]

Bodenschatz N, Brandes A, Liemert A, Kienle A. Journal of biomedical optics. 2014; 19(7):071405–071405. [PubMed: 24474551]

Bodenschatz N, Krauter P, Nothelfer S, Foschum F, Bergmann F, Liemert A, Kienle A. Journal of biomedical optics. 2015; 20(11):116006–116006. [PubMed: 26590206]

Bohren, CF., Huffman, DR. Absorption and scattering of light by small particles. John Wiley & Sons; 2008.

Bosschaart N, Edelman GJ, Aalders MC, van Leeuwen TG, Faber DJ. Lasers in medical science. 2014; 29(2):453–479. [PubMed: 24122065]

Buchholz TA, Somerfield MR, Griggs JJ, El-Eid S, Hammond MEH, Lyman GH, Mason G, Newman LA. Journal of clinical oncology. 2014; 32(14):1502–1506. [PubMed: 24711553]

Conklin MW, Eickhoff JC, Riching KM, Pehlke CA, Eliceiri KW, Provenzano PP, Friedl A, Keely PJ. The American journal of pathology. 2011; 178(3):1221–1232. [PubMed: 21356373]

Cuccia DJ, Bevilacqua F, Durkin AJ, Ayers FR, Tromberg BJ. Journal of biomedical optics. 2009; 14(2):024012–024012. [PubMed: 19405742]

Cuccia DJ, Bevilacqua F, Durkin AJ, Tromberg BJ. Opt. Lett. 2005; 30(11):1354–1356. [PubMed: 15981531]

Dehghani H, Eames ME, Yalavarthy PK, Davis SC, Srinivasan S, Carpenter CM, Pogue BW, Paulsen KD. Communications in Numerical Methods in Engineering. 2009; 25(6):711–732.

DAndrea C, Ducros N, Bassi A, Arridge S, Valentini G. Biomedical optics express. 2010; 1(2):471–481. [PubMed: 21258482]

Erickson-Bhatt SJ, Nolan RM, Shemonski ND, Adie SG, Putney J, Darga D, McCormick DT, Cittadine AJ, Zysk AM, Marjanovic M, et al. Cancer research. 2015; 75(18):3706–3712. [PubMed: 26374464]

Fedorov A, Beichel R, Kalpathy-Cramer J, Finet J, Fillion-Robin JC, Pujol S, Bauer C, Jennings D, Fennessy F, Sonka M, et al. Magnetic resonance imaging. 2012; 30(9):1323–1341. [PubMed: 22770690]

Fisher B, Anderson S, Bryant J, Margolese RG, Deutsch M, Fisher ER, Jeong JH, Wolmark N. New England Journal of Medicine. 2002; 347(16):1233–1241. [PubMed: 12393820]

Friebel M, Roggan A, Müller G, Meinke M. Journal of biomedical optics. 2006; 11(3):034021–034021.

Gélébart B, Tinet E, Tualle JM, Avrillier S. Pure and Applied Optics: Journal of the European Optical Society Part A. 1996; 5(4):377.

Gioux S, Mazhar A, Lee BT, Lin SJ, Tobias AM, Cuccia DJ, Stockdale A, Oketokoun R, Ashitate Y, Kelly E, et al. Journal of biomedical optics. 2011; 16(8):086015–086015. [PubMed: 21895327]

Jermyn M, Ghadyani H, Mastanduno MA, Turner W, Davis SC, Dehghani H, Pogue BW. Journal of Biomedical Optics. 2013; 18(8):086007–086007.

Kanick SC, McClatchy DM, Krishnaswamy V, Elliott JT, Paulsen KD, Pogue BW. Biomedical optics express. 2014; 5(10):3376–3390. [PubMed: 25360357]

Kanick S, Krishnaswamy V, Gamm U, Sterenborg H, Robinson D, Amelink A, Pogue B. Biomedical optics express. 2012; 3(5):1086–1100. [PubMed: 22567598]

Kanick S, Robinson D, Sterenborg H, Amelink A. Biomedical optics express. 2012; 3(1):137–152. [PubMed: 22254174]

Kaufman Z, Paran H, Haas I, Malinger P, Zehavi T, Karni T, Pappo I, Sandbank J, Diment J, Allweis T. BMC medical imaging. 2016; 16(1):57. [PubMed: 27724884]

Konecky SD, Rice T, Durkin AJ, Tromberg BJ. Journal of biomedical optics. 2011; 16(12):126001–1260018. [PubMed: 22191918]

Krishnaswamy V, Elliott JT, McClatchy DM, Barth RJ, Wells WA, Pogue BW, Paulsen KD. Journal of biomedical optics. 2014; 19(7):070504–070504. [PubMed: 25057960]

Laughney AM, Krishnaswamy V, Rizzo EJ, Schwab MC, Barth RJ Jr, Cuccia DJ, Tromberg BJ, Paulsen KD, Pogue BW, Wells WA. Breast Cancer Res. 2013; 15(4):R61. [PubMed: 23915805]

Laughney AM, Krishnaswamy V, Rizzo EJ, Schwab MC, Barth RJ, Pogue BW, Paulsen KD, Wells WA. Clinical Cancer Research. 2012; 18(22):6315–6325. [PubMed: 22908098]

McClatchy DM, Hoopes PJ, Pogue BW, Kanick SC. Journal of biophotonics. 2017; 10(2):211–216. [PubMed: 27807933]

McClatchy DM, Rizzo EJ, Wells WA, Cheney PP, Hwang JC, Paulsen KD, Pogue BW, Kanick SC. Optica. 2016; 3(6):613–621. [PubMed: 27547790]

Michels R, Foschum F, Kienle A. Optics Express. 2008; 16(8):5907–5925. [PubMed: 18542702]

Open Source Computer Vision Library. [Accessed June 2016] **URL:**https://github.com/itseez/opencv

Pardo A, Real E, Krishnaswamy V, López-Higuera JM, Pogue BW, Conde OM. IEEE Transactions on Medical Imaging. 2017; 36(1):64–73. [PubMed: 27479956]

Pleijhuis RG, Graafland M, de Vries J, Bart J, de Jong JS, van Dam GM. Annals of Surgical Oncology. 2009; 16(10):2717–2730. [PubMed: 19609829]

Provenzano PP, Eliceiri KW, Campbell JM, Inman DR, White JG, Keely PJ. BMC medicine. 2006; 4(1):38. [PubMed: 17190588]

Radosevich AJ, Eshein A, Nguyen TQ, Backman V. Journal of biomedical optics. 2015; 20:097002. [PubMed: 26414387]

Rogers JD, Çapoğlu İR, Backman V. Optics letters. 2009; 34(12):1891–1893. [PubMed: 19529738]

Sibai M, Veilleux I, Elliott JT, Leblond F, Wilson BC. Biomed Opt Express. 2015; 6(12):4923–4933. [PubMed: 26713206]

Smith T, Guild J. Transactions of the optical society. 1931; 33(3):73.

St John ER, Al-Khudairi R, Ashrafian H, Athanasiou T, Takats Z, Hadjiminas DJ, Darzi A, Leff DR. Annals of Surgery. 2017; 265(2):300–310. [PubMed: 27429028]

Taka SJ, Srinivasan S. Journal of Digital Imaging. 2011; 24(6):1103–1111. [PubMed: 21274590]

Tang R, Buckley JM, Fernandez L, Coopey S, Aftreth O, Michaelson J, Saksena M, Lei L, Specht M, Gadd M, Yagi Y, Rafferty E, Brachtel E, Smith BL. Breast cancer research and treatment. 2013; 139:311–316. [PubMed: 23670129]

Tang R, Saksena M, Coopey SB, Fernandez L, Buckley JM, Lei L, Aftreth O, Koerner F, Michaelson J, Rafferty E, Brachtel E, Smith BL. The British journal of radiology. 2016; 89:20150581. [PubMed: 26568439]

Tao YK, Shen D, Sheikine Y, Ahsen OO, Wang HH, Schmolze DB, Johnson NB, Brooker JS, Cable AE, Connolly JL, et al. Proceedings of the National Academy of Sciences. 2014; 111(43):15304–15309.

Tse G, Tan PH, Pang AL, Tang AP, Cheung HS. Journal of clinical pathology. 2008; 61(2):145–151. [PubMed: 17704264]

Wang Y, Kang S, Khan A, Ruttner G, Leigh SY, Murray M, Abeytunge S, Peterson G, Rajadhyaksha M, Dintzis S, et al. Scientific reports. 2016; 6

Wong TT, Zhang R, Hai P, Zhang C, Pleitez MA, Aft RL, Novack DV, Wang LV. Science Advances. 2017; 3(5):e1602168. [PubMed: 28560329]

Zhao Y, Tabassum S, Piracha S, Nandhu MS, Viapiano M, Roblyer D. Biomed Opt Express. 2016; 7(6):2373–2384. [PubMed: 27375952]

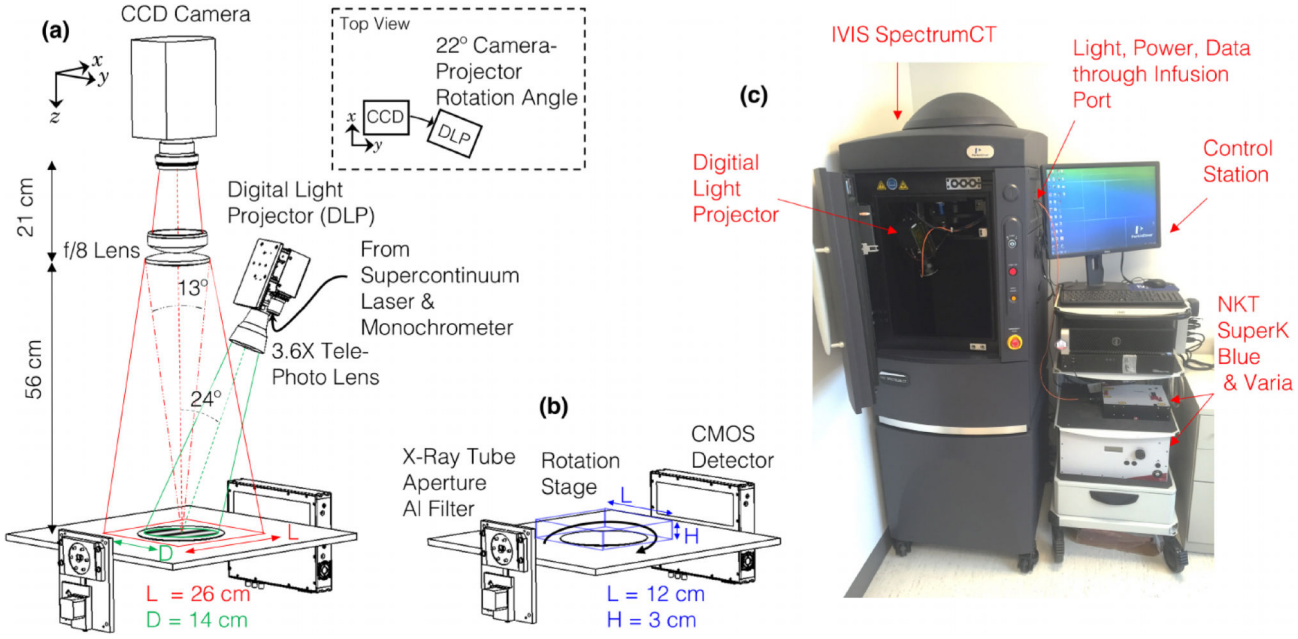

Figure 1.

Schematics of the major components of the SLI and micro-CT systems are labeled in (a) and (b), respectively. A photograph of the system located in the gross specimen processing lab is shown in (c). The system is self-shielded and house in a mobile form factor as shown in (c). There is a maximum radiation exposure of ≤ 0.01 mR/hr above background during operation.

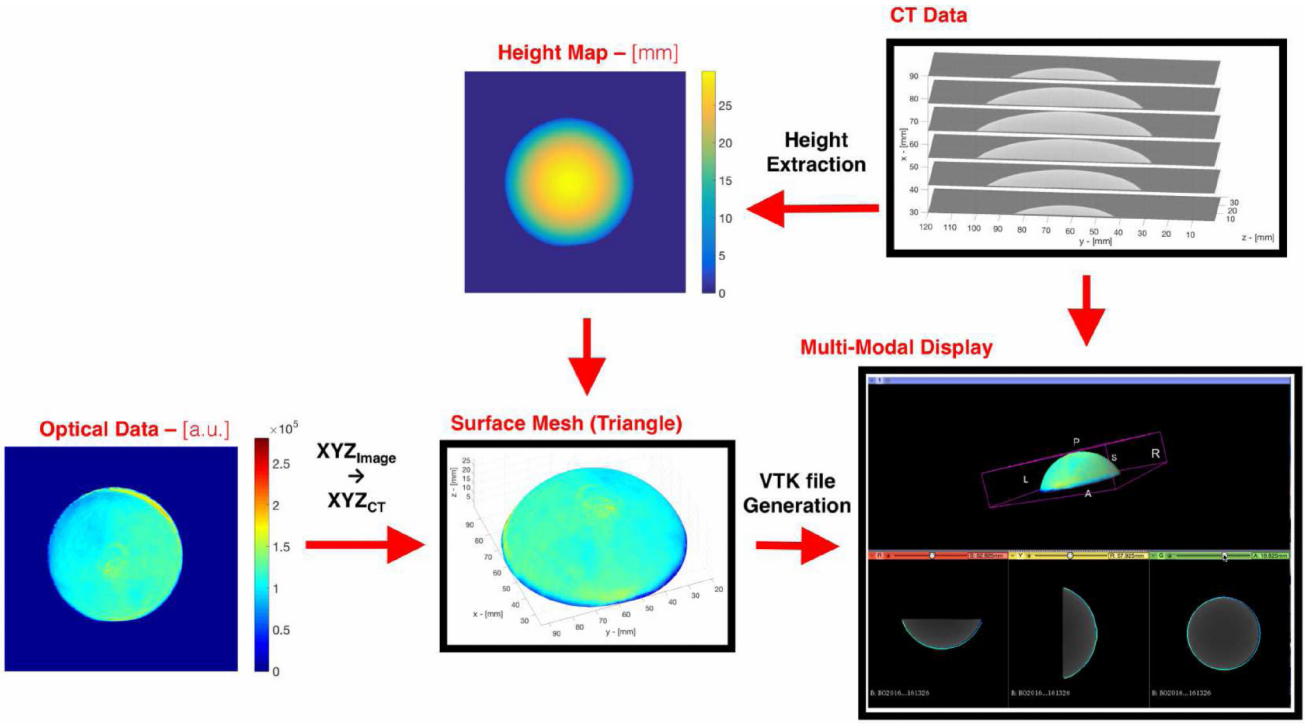

Figure 2.

Flow diagram of the multimodal data processing and work-flow is shown for a hemispherical phantom. First, optical and CT data are sequentially acquired with the SLI/CT system. A height map is extracted from the CT and the optical data undergoes a coordinate transformation from image coordinates to CT coordinates, from which a 3D surface mesh is created as a VTK file. Both the VTK file and CT DICOM can be simultaneously rendered in the open source Slicer environment, shown in the bottom right view.

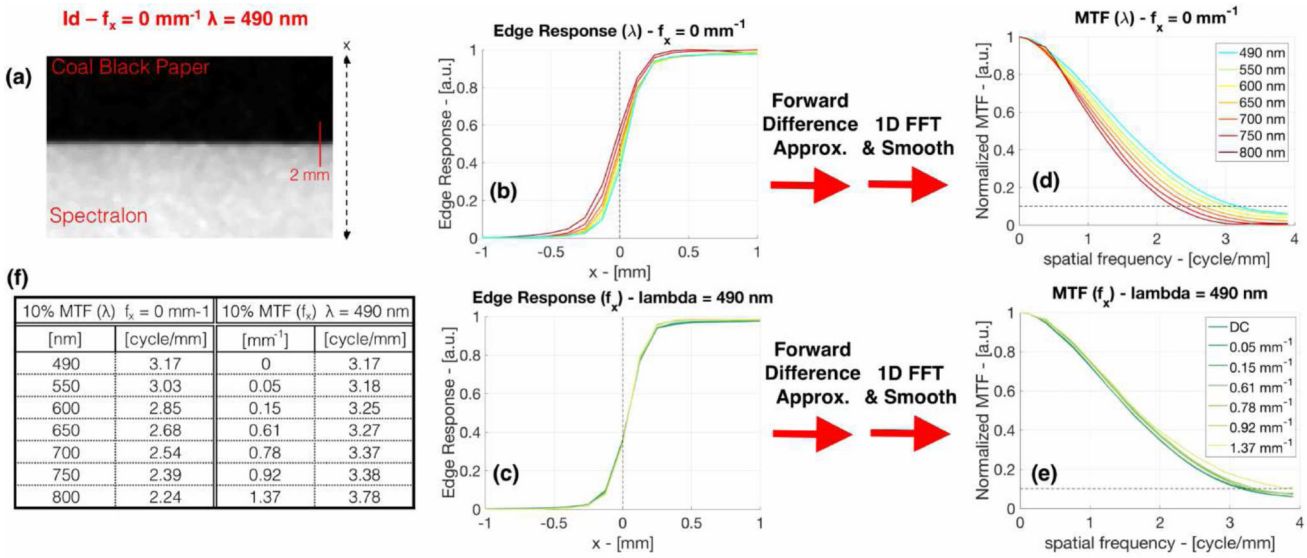

10% MTF (λ) f_x = 0 mm-1		10% MTF (f_x) λ = 490 nm	
[nm]	[cycle/mm]	[mm^{-1}]	[cycle/mm]
490	3.17	0	3.17
550	3.03	0.05	3.18
600	2.85	0.15	3.25
650	2.68	0.61	3.27
700	2.54	0.78	3.37
750	2.39	0.92	3.38
800	2.24	1.37	3.78

Figure 3.

(a) Diffuse image of the step phantom at λ = 490 nm. Edge response functions (ERF) are shown in (b) for each sampled wavelength at f_x = 0 mm^{-1} and (c) for each sampled spatial frequency at λ = 490 nm. Corresponding modulated transfer functions (MTF) appear in (d) and (e), as the Fourier Transform of the derivative of the ERF. In (f), the limiting cycles per mm at 10% of the max MTF are tabulated.

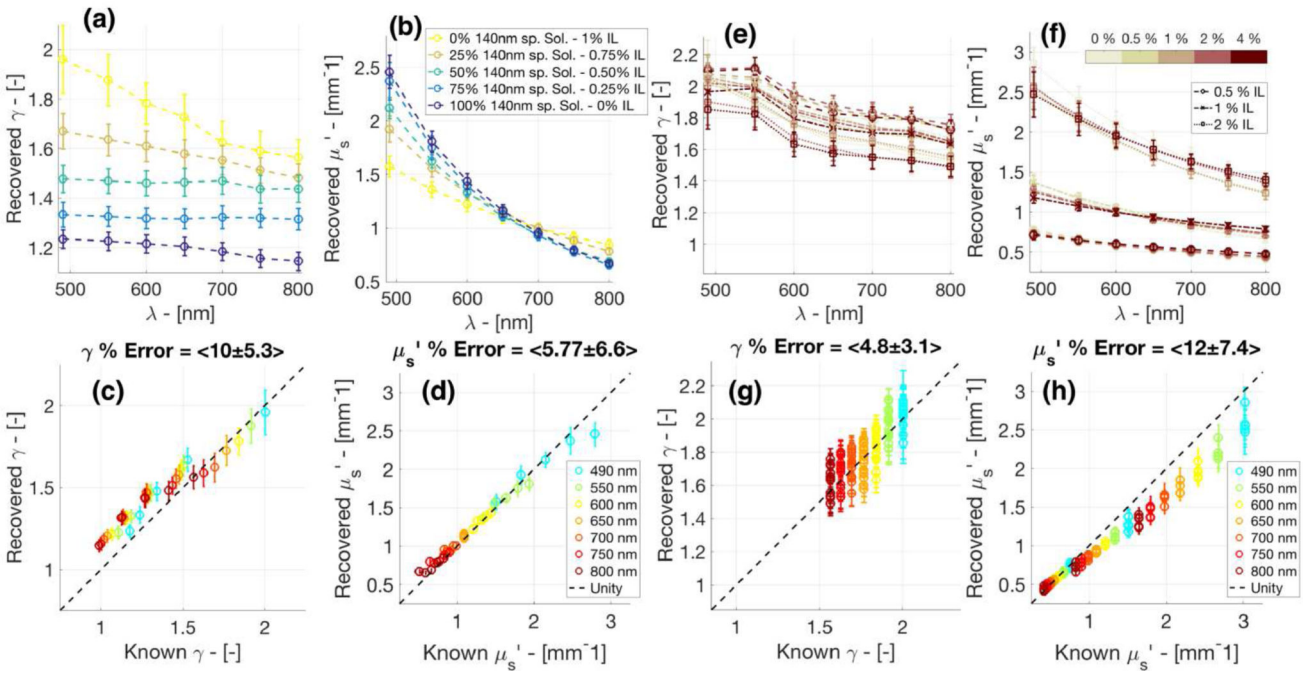

Figure 4.

A summary of optical property recovery data is shown. In (a) and (b), respectively, the recovered phase function parameter, γ, and recovered reduced scattering coefficient, μ_s', appear as functions of wavelength for the various concentrations of Intralipid (IL) and a solution of 140 nm spheres. Clear stratification between each particle size-scale distribution occurs in the magnitude of γ and the spectral slope of μ_s'. In (c) and (d), known versus recovered plots are shown for γ and μ_s', respectively, over all wavelengths for the various particle size-scale distribution. The recovered values of γ and μ_s' versus wavelength are presented in (e) and (f) respectively, for the various blood volume fractions (BVF) and IL concentrations. In (g) and (h), known versus recovered plots are displayed for γ and μ_s', respectively, over all wavelengths for the various BVF and IL concentrations. Error-bars represent one standard deviation within the measured region of interest (ROI) for each phantom well.

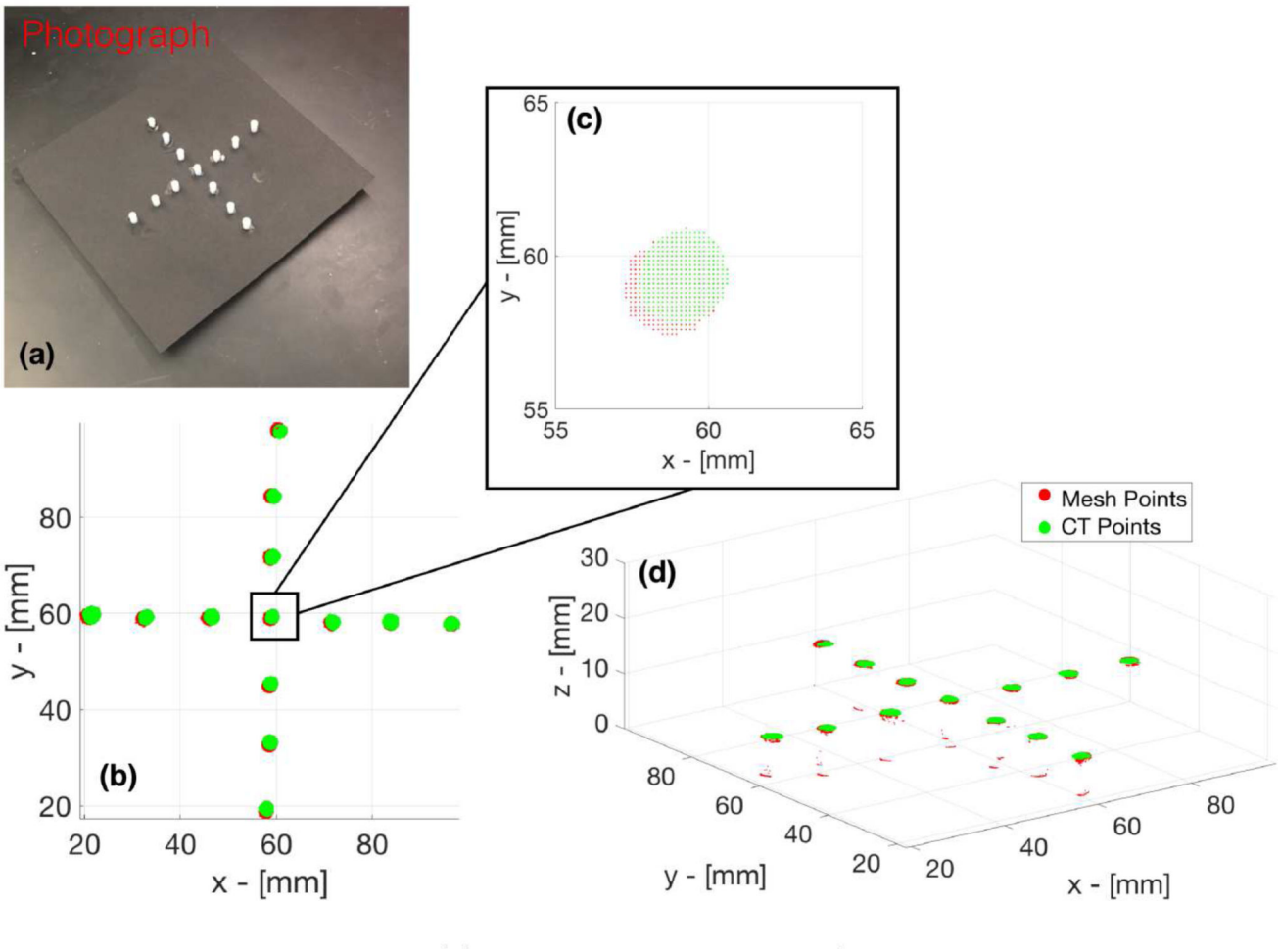

Figure 5.

In (a), the photograph of CT/Optical co-registration phantom is shown. In (b), the 2D XY plane view of the segmented CT and co-registered optical mesh points is presented, with a zoomed-in view of the center marker in (c). In (d), the same segmented CT and co-registered optical pixels are displayed in 3D space.

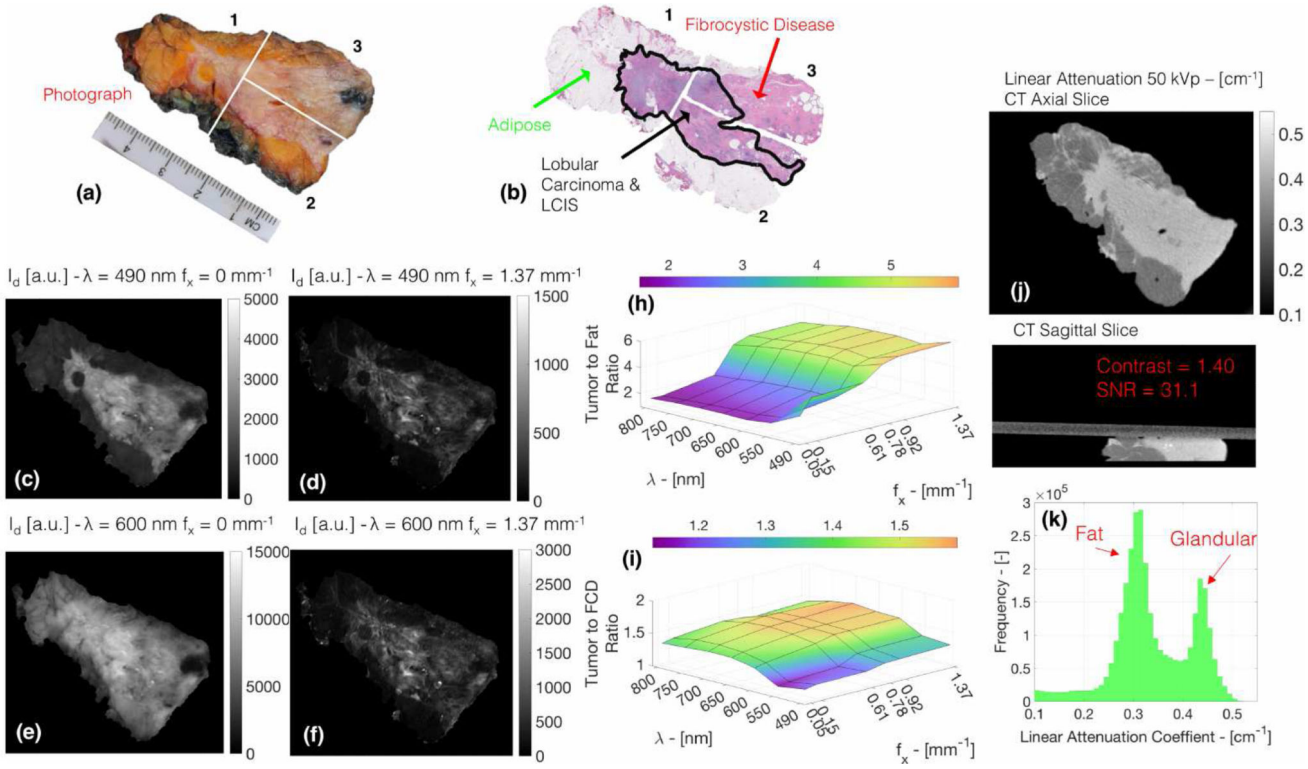

Figure 6.

In (a), a photograph of the resected breast specimen is shown, with white lines indicating where the specimen was cut for histological processing. In (b), tessellated H&E sections of the specimen appear with a malignant region outlined in black. Demodulated images of f_x = [0, 1.37] mm^{-1} for λ = [490, 600] nm are presented in (c–f), with the tissue specimen segmented from the background. For the areas of tumor, FCD, and adipose marked by arrows in (b), surfaces of ratios in the demodulated intensity between tumor to fat and tumor to FCD over spatial frequency and wavelength are shown in (h) and (i), respectively. Axial and sagittal cross sections of the linear attenuation coefficient are displayed in (j) for a 50 kVp micro-CT scan of the specimen. A histogram of the reconstructed linear attenuation coefficient values of the breast tissue specimen is shown in (k), where an apparent bimodal distribution is observed with separate fat and glandular peaks.

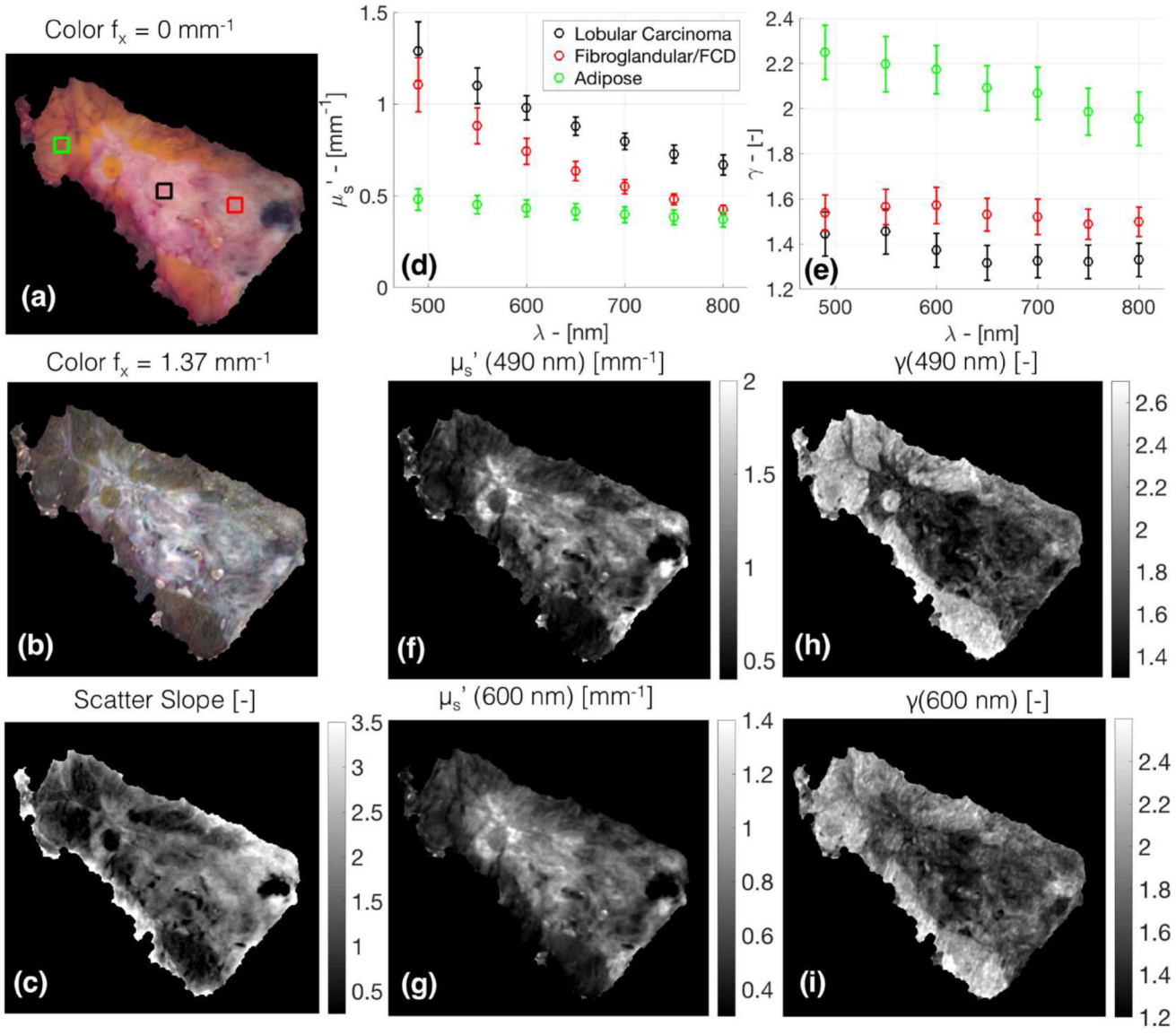

Figure 7.

A summary of reconstructed SLI data of the segmented tissue specimen is shown. Color images, reconstructed from multi-spectral SLI data at f_x = [0, 1.37] mm^{-1} appear in (a) and (b), respectively. An image of the spectral slope of μ_s' is presented in (c). Black, red, and green boxes in (a) outline regions of lobular carcinoma, fibrocystic disease, and adipose. The means within each region of μ_s' and γ are plotted as a function of wavelength in (d) and (e), respectively, with error-bars representing the standard deviation within the region. Maps of μ_s' are shown in (f) and (g) and maps of γ appear in (h) and (i) for λ = 490 nm and 600 nm, respectively.

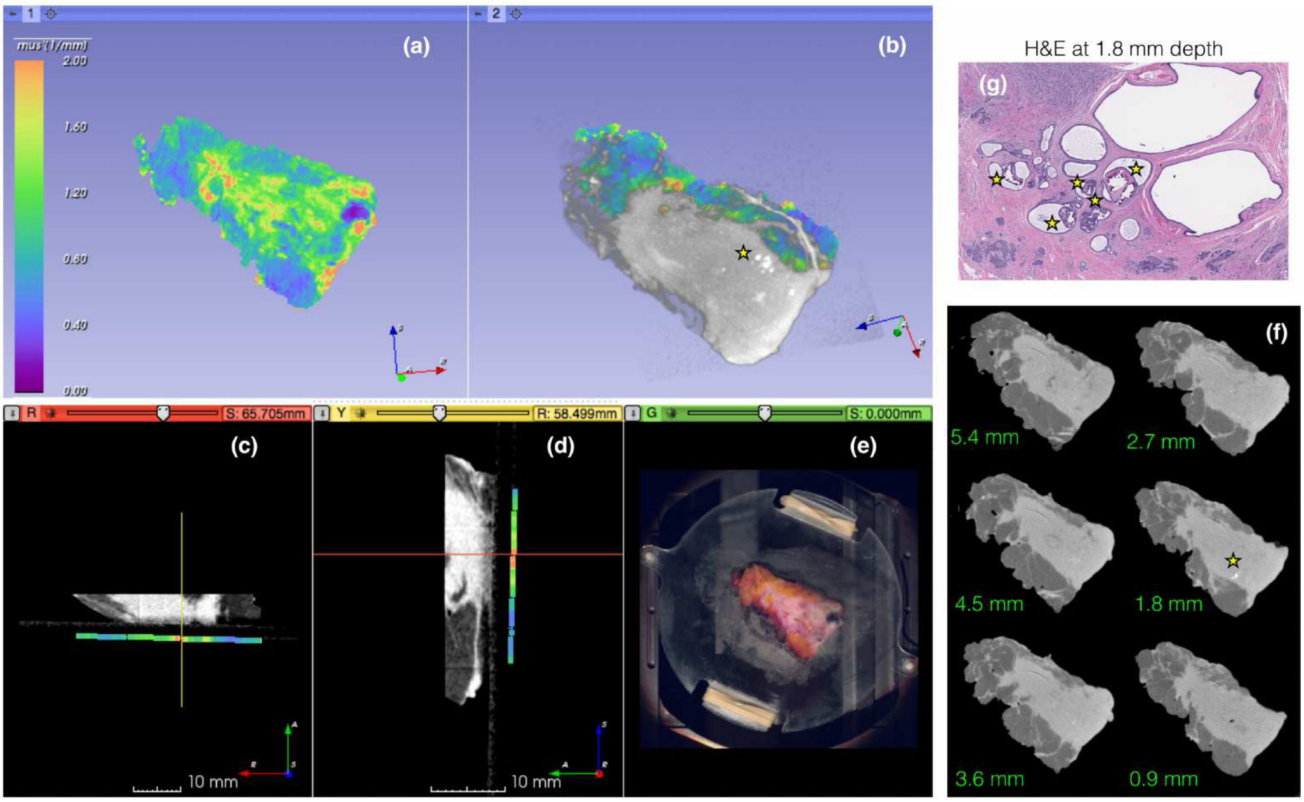

Figure 8.

Multimodal display of the resected breast specimen using NIRFAST Slicer. In panel (a), the μ_s' surface is shown, while in panel (b), the μ_s' surface is co-registered to the MIP volume of the micro-CT is shown. In panels (c) and (d), the sagittal and coronal planes of the co-registered μ_s' surface and micro-CT volume are presented. In panel (e), a diffuse reconstructed color image of the specimen in the acrylic holder is shown. In (f), various axial slices of the micro-CT are displayed in 0.9 mm increments below the imaging surface. In the MIP volume and in the micro-CT slice at 1.8 mm below the imaging surface, micro-calcifications appear as a cluster of white specs, which are marked with a yellow star. In (g), an H&E section taken at 1.8 mm depth corroborate the presence of micro-calcifications. A cluster of type-II calcifications can be seen and are marked with yellow stars.

Table 1

Summary of micro-CT performance metrics and size of minimum detectable objects (MDO) in the mammography target phantom.

	SNR	Contrast	Exposure Time [sec]	$Fiber_{MDO}$ [mm diameter]	$Specks_{MDO}$ [mm diameter]	$Masses_{MDO}$ [mm thick]
25 kVp	23.8	1.81	144	0.54	0.24	0.25
50 kVp	34.0	1.64	72	0.54	0.24	0.25

Table 2

Optical micro-CT co-registration accuracy. Mean distances between centroids of phantoms for CT points and Image mesh points with varying phantom locations.

	Center Phantom (n=1)	1 cm from Center (n=4)	2 cm from Center (n=4)	3 cm from Center (n=4)	Total (n=13)
$\Delta C = \lvert C_{CT} - C_{Mesh} \rvert$ [mm]	0.7	0.6 ± 0.2	0.6 ± 0.3	0.6 ± 0.4	0.6 ± 0.3

Phys Med Biol. Author manuscript; available in PMC 2018 November 10.